Investigating physics-informed neural networks for heat flux estimation: a sensitivity analysis towards Wendelstein 7-X applications

Plasma Physics and Controlled Fusion

OPEN ACCESS

RECEIVED
2 February 2026

REVISED
5 May 2026

ACCEPTED FOR PUBLICATION
2 June 2026

PUBLISHED
15 June 2026

PAPER

Investigating physics-informed neural networks for heat flux estimation: a sensitivity analysis towards Wendelstein 7-X applications

Enrico Aymerich[1,*], **Fabio Pisano**[1], **Giuliana Sias**[1], **Barbara Cannas**[1], **Alessandra Fanni**[1], **Joris Fellinger**[2], **Yu Gao**[2], **Marcin Jakubowski**[2], **Sebastian Thiede**[2] and **W7-X Team**[3]

[1] Department of Electrical and Electronic Engineering, University of Cagliari, Cagliari, Italy
[2] Max-Planck-Institut für Plasmaphysik, Greifswald, Germany
[3] see authors: O Grulke, *et al* Nuclear Fusion, 2024, 64 (11), 112 002.
[*] Author to whom any correspondence should be addressed.

E-mail: enrico.aymerich@unica.it

Keywords: neural networks, heat flux estimation, physics-informed, W7-X, divertor, heat equation

Abstract

Real-time estimation of divertor heat loads is critical for plasma-facing component protection in Wendelstein 7-X (W7-X). The current heat-flux reconstruction tool, THEODOR, is too computationally demanding for real-time use, motivating the development of faster physics-based surrogates. Physics-informed neural networks (PINNs) have recently been shown to model the heat equation and the associated heat-flux partial differential equation, though only for fixed boundary and initial conditions, when the heat potential profile at the top of the tile is represented as a Gaussian function. This choice is motivated by the observation that experimental profiles can be well approximated by a small number of Gaussian peaks in the strike-line region. Within this framework, the present work extends the PINN framework by assessing the sensitivity of the PDE solution to variations in the boundary and initial conditions, using a synthetic dataset with Gaussian boundary-condition profiles. Two approaches are investigated: (i) training multiple PINNs for different initial tile temperatures and Gaussian boundary-condition parameters; (ii) developing a parameterized PINN capable of solving the PDE across a continuous range of conditions. This approach demonstrates the feasibility of PINN-based heat-flux reconstruction with improved flexibility, in view of the application with real-time experimental data at W7-X.

1. Introduction

Wendelstein 7-X is a landmark experiment in fusion research, designed to demonstrate that optimized stellarators can sustain steady-state, reactor-relevant operation. Its achievements in plasma confinement, magnetic field precision, and reactor-scale engineering mark significant progress toward practical fusion energy [1, 2]. Managing heat fluxes on the divertor is a central challenge for W7-X, since steady-state operation requires robust protection of plasma-facing components. The island divertor concept addresses this by achieving large wetted areas and broad strike lines, lowering peak heat fluxes compared with typical tokamaks [3, 4]. Moreover, the upgrade of the inertially cooled divertor with a water-cooled one contributed to the W7-X performance increase leading to the recent campaign results [5].

Most of the exhaust power is deposited on the divertor plates, while the distribution depends sensitively on magnetic configuration, plasma pressure, and equilibrium effects [4, 6]. At higher plasma densities, W7-X has demonstrated robust detachment, where divertor heat flux drops by more than an order of magnitude, establishing a stable and reactor-relevant exhaust regime [7, 8].

These advances show that the island divertor can safely handle high-power and long-pulse operation. At the same time, the experimental campaigns investigated the complexity and variability of heat flux patterns, which evolve with configuration and plasma state. Timely characterization and control of heat loads are therefore essential for reliable steady state performance, as well as an improvement in cooling

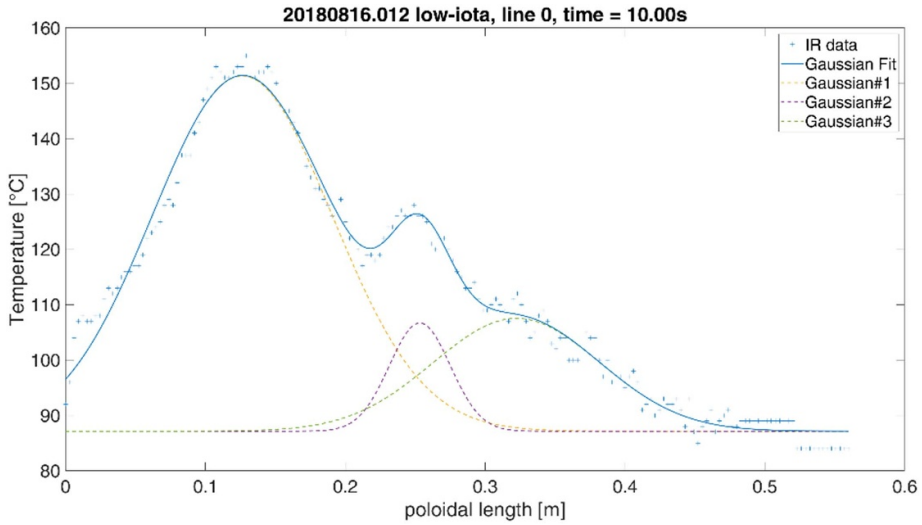

Figure 1. Experimental IR data from shot 20 180 816.012, low-iota divertor, line 0 at time 10 s and its fit (full blue line) using a sum of Gaussians. The different Gaussians composing the fit are represented with dashed lines.

performance. While advanced diagnostics provide detailed measurements, heat-flux real-time estimation remains an open challenge. Machine learning and thermography-based approaches are being developed to meet this need [9–11], providing a pathway toward predictive divertor monitoring and active heat-flux control in future campaigns.

In this context, physics-informed neural networks (PINNs) are a valuable tool for real-time heat flux estimation, especially in complex systems with complex geometries like W7-X, where traditional numerical methods can be too slow for operational control. PINNs incorporate the heat equation and relevant boundary/initial conditions directly into the neural network's loss function. This allows the network to learn the underlying physics without requiring large experimental datasets, enabling rapid and accurate heat flux predictions even with noisy or incomplete data. Traditional codes (e.g. THEODOR [11, 12]), which solve the heat equation offline are computationally intensive, despite some effort to develop efficient real-time versions for real-time [13]. On the other hand, PINNs can be easily ported on GPU hardware and parallelized to estimate heat fluxes on divertor tiles in real time, making them suitable for feedback and control during plasma experiments [9]. A new approach based on PINNs was proposed in [9] to develop a tool capable of computing the heat equation solution and the heat fluxes partial differential equation (PDE) in real time. However, the PINN only solved the PDE considering a fixed boundary and initial condition, considering only a tile with initial temperature of 25 °C and a top Gaussian with 2000 °C of peak temperature centered in the middle of the tile width and with 0.056 m of standard deviation. This choice was motivated by the observation that a good approximation of the experimental profiles at the top of the tile can be obtained as a combination of a few Gaussians, with one or two peaks in the strike-line region. For instance, in figure 1 an example profile from experiment 20 180 616.012 is shown, coming from the low iota region of the divertor module. The crosses indicate the experimental datapoints and the continuous line a Gaussian fitting with three Gaussians, with the highest one (yellow dashed line) having amplitude of 64.20 °C, center μ of 0.1264 [m] and σ of 0.064 [m].

In this paper, an extension of the PINN approach is investigated by studying the influence of the boundary and initial conditions on the performance of the PDE solution. In this context, a sensitivity analysis of the proposed architecture has been made by training several PINNs when varying the initial uniform temperature T_0 of the tile, together with the center (μ) and spread (σ) of the Gaussian temperature boundary condition on the tile surface. This simplified approach, with a single Gaussian, helps to easily assess the possibility of generalization of the PINN in view of a real-time application at W7-X. Using the (μ, σ, T_0) *parameters the Dirichlet boundary condition at the top of the tile can be expressed as in* equation (1)

$$\hat{T}(0,y,t) = T_{\mathrm{bD}}(y,t) = \frac{t}{0.01}\left(200\mathrm{e}^{-\frac{(y-\mu)^2}{2\sigma^2}}\right) + T_0. \tag{1}$$

Then, a parameterized PINN, capable of solving the heat flux PDE for different initial and boundary conditions, is proposed. In this case, the parameters (T_0, μ_0, σ), previously scanned, are provided as

input to the PINN. Furthermore, the workflow towards implementing a real-time PINN solution for W7-X operations is presented, discussing the strategy for tailoring the parametric PINN to real-world data. Indeed, by processing experimental IR data from W7-X, a dataset of suitable boundaries and initial conditions can be created. Once complete, such dataset would allow the development of parametric PINNs able to work with experimental IR data. This advancement aims to bridge the gap between offline modeling and real-time application, developing tools for W7-X's operational safety and efficiency.

In section 2, the methodology of the work is described, starting with the transient heat diffusion problem and discussing the single case and the parametric PINN approach. Section 3 details the results of the PINN models proposed, and Section 4 concludes the work.

2. Methodology

This section details the heat diffusion model solved by the PINN model in terms of the PDE equation and its constraints. Figure 2 shows a sketch of the divertor tile with the coordinate system used in this work. This work compares the PINN with the code and approach used during inertially cooled divertor campaign OP1.2 (2017–2018) based on THEODOR for the 2D heat diffusion equation solution. In this work, a tile 0.56 m wide and 0.028 m thick is considered.

2.1. Heat flux calculation

To compute the heat flux entering the divertor tile, the code needs to solve the heat diffusion equation:

$$\frac{\partial u}{\partial t} = D(u)\left(\frac{\partial^2 u}{\partial x^2} + \frac{\partial^2 u}{\partial y^2}\right). \tag{2}$$

In equation (1), u is the heat potential, dependent on the temperature T, and defined as:

$$u(T) = \int_{0\,^\circ C}^{T} k(T)\,\mathrm{d}T \tag{3}$$

where $k(T)$ is the thermal conductivity coefficient. Moreover, $D(u)$ is the heat diffusion coefficient, which is dependent on the heat potential and thus on the temperature of the material. Regarding the system of coordinates, x is the direction along the tile depth, y is the poloidal direction, as depicted in the tile sketch of figure 2.

In this formulation, the heat diffusion along z direction is neglected due to the presence of a homogeneous distribution of the strike line in finite toroidal range, as also reported in [11]. This simplification is also the same for THEODOR and prevents from considering shaping effects such as slits between the divertor tiles. Moreover, for the purpose of this work, the effect of surface layers is neglected [14].

For the measurement of the heat fluxes during the experiment, several heat diffusion problems must be solved, in order to track the state of the tile during the experiment. Firstly, an assumption on the initial condition of the bulk of the tile is made. Then, the IR temperature measurement of the surface tile enforces the top Dirichlet boundary condition of the heat diffusion problem, together with the Neumann adiabatic condition at the lateral sides of the tile. The initial condition can be either assumed as a uniform constant temperature (at the beginning of the experiment) or reconstructed from the previous frames (during the experiment). For the heat flux reconstruction in a full experiment, the heat diffusion solver computes the temperature evolution for one timestep, then the state of the tile at the end of the heat diffusion is used as initial condition for another diffusion problem, which uses the updated IR temperature measurement as top boundary condition. In this paper, the same conditions are assumed when using the PINN implementation, but the heat flux physics informed neural network (*HF-PINN*) performance is evaluated on the single timestep reconstruction only.

2.2. HF-PINN

Physics informed NN can be trained to numerically solve PDEs by including physics-based criteria in the loss function. The physics informed models exploit the possibility of calculating the gradient of the output with respect to the input. A sketch of a PINN is shown in figure 3(a). In this case, the model is trained using as input the spatial position and time instant at which the solution is to be calculated, while the function to be minimized is based on the PDE in equation (2). Moreover, to make the solution unique, also the surface boundary condition, the lateral boundary condition and the initial conditions are included in the model loss. In this way it is possible to constrain the output function of the NN to solve the differential equation without using reference data.

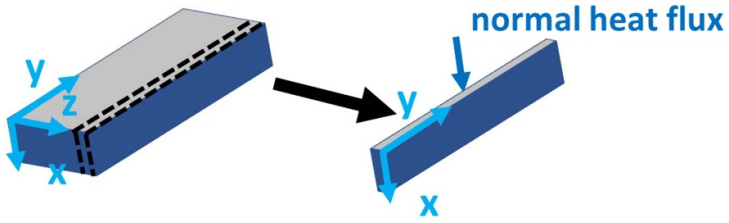

Figure 2. Left: sketch of the divertor tile, where x is the direction along the tile depth; y is the direction along the tile length (poloidal direction); z is the toroidal direction. Dashed lines segment a profile, the computational domain of the PDE. Right: sketch of the poloidal profile with arrow indicating the direction of the normal heat flux from the plasma.

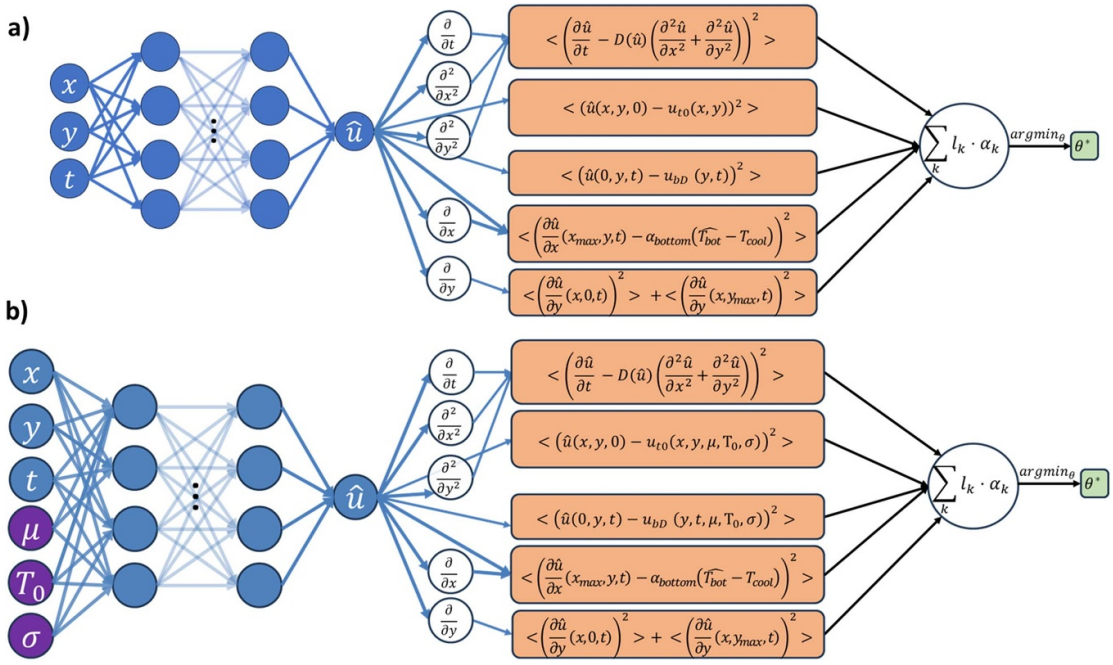

Figure 3. a) Scheme of *HF-PINN$_{one\text{-}case}$*, which finds the solution of a non-parametric diffusion equation; b) Scheme of *HF-PINN$_{param}$* which includes μ, T_0, σ as additional input parameters to solve a parametric PDE.

In this context, the loss function (L) of the PINN can be written as a weighted sum of several contributions:

$$L = \alpha_{\mathrm{PL}} L_{\mathrm{PDE}} + \alpha_{\mathrm{IC}} L_{t0} + \alpha_{By} L_{\mathrm{bN}} + \alpha_{Bx_{\mathrm{top}}} L_{\mathrm{bD}} + \alpha_{Bx_{\mathrm{bot}}} L_{\mathrm{bR}} \tag{4}$$

where L_{PDE} is the mean squared error (MSE) on the approximation of the PDE (Physics loss), L_{t0} is the MSE with respect to the value of the initial condition, L_{bN}, L_{bD} and L_{bR} are the MSEs with respect to the value of each boundary condition, Neumann, Dirichlet and Robin respectively. Among the three conditions, L_{bN} is the Neumann boundary condition loss imposing adiabaticity at the tile edges, L_{bD} is the Dirichlet boundary condition loss imposing the temperature at the top of the tile and L_{bR} is the condition modeling the convective heat exchange with the inertially cooled divertor of W7-X installed during OP1.2. The contributions to the loss are the same as defined in (4) of [9], and a Robin condition loss is included at the bottom of the tile, as reported below for the sake of clarity:

$$L_{\mathrm{PDE}} = \mathrm{MSE}\left(\frac{\partial \hat{u}}{\partial t}(x,y,t), D(\hat{u}(x,y,t))\left(\frac{\partial^2 \hat{u}}{\partial x^2}(x,y,t) + \frac{\partial^2 \hat{u}}{\partial y^2}(x,y,t)\right)\right) \tag{5}$$

$$L_{t0} = \mathrm{MSE}\left(\hat{u}(x,y,0), u_{t0}(x,y)\right) \tag{6}$$

$$L_{\mathrm{bN}} = \mathrm{MSE}\left(\frac{\partial \hat{u}}{\partial y}(x,0,t), 0\right) + \mathrm{MSE}\left(\frac{\partial \hat{u}}{\partial y}(x,y_{\max},t), 0\right) \tag{7}$$

Table 1. Parameter values scanned for the sensitivity analysis of *HF-PINN$_{one\text{-}case}$*.

Parameter	Description	Values
μ	Center of Gaussian on top condition	$[0.056, 0.168, 0.28]$ m
σ	Standard deviation of Gaussian on top condition	$[0.056, 0.112, 0.28]$ m
T_0	Initial uniform tile temperature	$[25, 100, 200]^\circ$ C

$$L_{\mathrm{bD}} = \mathrm{MSE}\left(\hat{u}\left(0, y, t\right), u_{\mathrm{bD}}\left(y, t\right)\right) \tag{8}$$

$$L_{\mathrm{bR}} = \mathrm{MSE}\left(\frac{\partial \hat{u}}{\partial x}\left(x_{\max}, y, t\right), \alpha_{\mathrm{bottom}}\left(\hat{T}\left(x_{\max}, y, t\right) - T_{\mathrm{cool}}\right)\right) \tag{9}$$

where

$$\mathrm{MSE}\left(p, \hat{p}\right) = \left(p - \hat{p}\right)^2 \tag{10}$$

u_{t0} is the initial condition of the PDE, u_{bD} the Dirichlet boundary condition on the top of the tile and y_{bN} represents the lateral edges of the tile where the adiabatic condition is imposed. The values α_{PL}, α_{IC}, α_{By}, $\alpha_{Bx_{\mathrm{top}}}$ and $\alpha_{Bx_{\mathrm{bot}}}$ are the scalar weights of the loss terms. In equation (9), $\hat{T}(x_{\max}, y, t)$ is the temperature at the bottom of the tile, transformed from the heat potential $\hat{u}$ computed by the PINN, while the parameters $T_{\mathrm{cool}} = 20°\mathrm{C}$ and $\alpha_{bottom} = 200 W/\left(m^2\, K\right)$ help modeling the heat convection of the W7-X inertially cooled divertor installed during OP1.2, coherently with the THEODOR implementation [11].

Several works in the literature discuss the convergence of the PINN loss and the possibility to dynamically tune the weights to improve it [15, 16], but in this work a two-step approach is taken, firstly learning the behavior of the solution on the boundary of the domain then increasing the α_{PL} weight, as described in section 2.3. The gradual refinement of the model is applied also for other PINNs trained without target data [17]. In this work, the enforcement of the boundary and initial conditions is not exact, since the mismatch of the solution with the values at the boundaries is penalized by the loss, but not strictly enforced. Other approaches enforce the boundary condition by canceling the output of the network on the boundary of the domain. The boundary condition is then satisfied by a function that constrains the output to the values of the boundary conditions [18, 19].

2.3. Training setup and sensitivity analysis with HF-PINN$_{\mathbf{one\text{-}case}}$

The architecture of the model is a Feed-Forward NN with 10 hidden layers, each of them with 97 neurons, and with a hyperbolic tangent (*tanh*) activation function, as optimized in [9] by the same authors.

In [9] only the case where the Dirichlet boundary condition was a single Gaussian peaked at the center of the tile was analyzed. In this work, the top boundary condition has been parametrized as a Gaussian with given mean μ and spread σ. The initial condition, instead, is parametrized as a uniform temperature of T_0 in the bulk of the tile at $t = 0$ s. Note that, this assumption holds mostly at the initial frames of a W7-X experiment, and it is not representative of the tile conditions close to the end of the experiment, when the tile bulk has been heated not uniformly by the interaction with the plasma. However, since the tile diffusion properties depend on the temperature [11], the uniform initial temperature serves as a good starting point to explore the capability of the PINN model to adapt to different tile conditions. The limitations associated with this simplification will be addressed and removed in later developments.

Fixing the three temperature parameters (μ, σ, T_0), equation (1) describes the boundary condition on top of the tile between two IR frames as a Gaussian growing in time for $t \in [0, 0.01]$ s, with a peak value of 200 °C over the initial temperature of the tile T_0.

The boundary condition in (1) is rescaled from temperature into heat potential in (8) by using the equation (2). In the same way, also T_0 is rescaled to U_0 with (3) to be used in (6) as initial condition in the bulk of the tile. A more detailed description of this procedure is included in the Appendix A1.

Three values for each parameter have been included in the scan, for a total of 27 combinations. The parameters and their values are summarized in table 1. For this parametric scan, only values of μ less than or equal to 0.28 m, i.e. the center of the tile, have been taken into account assuming symmetrical conditions on the other side of the tile.

The training is performed in two steps. In the first step, a set of fixed collocation points is generated in the top part of the domain $x \in [0,\ 2.8]\, mm$, sampling 10 points with uniform spacing in x, 10 points with uniform spacing in time t and 80 points uniformly along the width of the tile. These anchor points

Table 2. Parameters range of *HF-PINN$_{param}$*.

Parameter	Description	Values
μ	Center of top condition	$\mathbb{R} \in [0, 0.56]$ m
σ	Standard deviation of top condition	$\mathbb{R} \in [0.056, 0.504]$ m
T_0	Initial uniform tile temperature	$\mathbb{R} \in [25, 800]^\circ$ C

are used to make the model focus on the volume of the domain where the solution is steeper. Moreover, other 10 000 points are selected randomly sampling the computational domain, 4000 in the top boundary ($x = 0$, y, t), where the Dirichlet condition is applied, 4000 in the bottom boundary ($x = x_{\max}$, y, t), where the Robin condition is imposed, and 400 in each of the y edges where the adiabatic boundary condition is enforced, on the surfaces (x, $y = 0$, t) and (x, $y = y_{\max}$, t). Other 1000 points are picked up within the tile to enforce the initial condition, in (x, y, $t = 0$). The random points are generated every 1000 iterations, while the same number of validation points is selected uniformly sampling the computational domain.

Each one of the 27 *HF-PINN$_{one\text{-}case}$* models is trained using the Adam optimizer, and the training is stopped after 50 000 epochs if the loss on the training set does not improve for 5000 iterations. In this first training step, the loss is the one defined in (3), where α_{IC} and $\alpha_{Bx_{\mathrm{top}}}$ are set to 1, α_{By} is set to 0.25, $\alpha_{Bx_{\mathrm{bot}}}$ is set to 0.001, and α_{PL} to 0.01. The model with the minimum validation loss is saved. Following to this training step, another one is performed with 60 000 epochs to refine the solution inside the domain, by increasing α_{PL} to 0.1 and decreasing α_{By} to 0.05 and $\alpha_{Bx_{\mathrm{bot}}}$ to 0.0002 without changing $\alpha_{Bx_{\mathrm{top}}}$ and α_{IC}. In each case, the loss is normalized dividing by the heat potential U_0 obtained from (3) when $T = T_0$, with T_0 the initial temperature of the tile.

In this way, in the first phase the training is focused on learning the initial and boundary conditions. In the second phase, the training is focused on learning the PDE behavior while enforcing the initial and boundary conditions.

2.4. Development of a parametrized model HF-PINN$_{\mathbf{param}}$

Each *HF-PINN$_{one\text{-}case}$* is trained to solve a specific example of the transient heat diffusion PDE, which is not suitable for the application to the W7-X real-time diagnostic system case when the experimental conditions vary and require the model to find a different solution to the PDE in equation (1) at each frame of the IR camera system. For this reason, a parametrized model which solves the different cases discussed in the previous section is proposed in this work. A preliminary approach for the creation of a parametric PINN (*HF-PINN$_{param}$*) shows that the same network can solve the heat equation with a set of diverse boundary conditions and initial conditions. figure 3(b) shows the architecture of *HF-PINN$_{param}$*, and the parameters, μ, σ, T_0 scan a higher range as detailed in table 2. The training follows the same two steps defined for *HF-PINN$_{one\text{-}case}$*, but in this case the anchor points are fixed in the top part of the domain $x \in [0, 2.8]$ mm, sampling 15 points with linear spacing in x, 80 points in t and 120 points in the entire width of the tile.

Also in this case, the evolution of the heat potential is learnt without including data from THEODOR in the training. The *HF-PINN$_{param}$* is trained in the same way as the *HF-PINN$_{one\text{-}case}$* in the first training step. Following this training step, another one is performed for 150 000 epochs to refine the solution inside the domain, by increasing α_{PL} to 0.1 and decreasing α_{By} to 0.05 and $\alpha_{Bx_{\mathrm{bot}}}$ to 0.0005 without changing $\alpha_{Bx_{\mathrm{top}}}$ and α_{IC}. For this model, the loss is normalized by the heat potential $U_{\min}$, obtained from equation (2) when $T = 25\,^\circ$C.

3. Results

3.1. Introduction

In the following, the results of the *HF-PINN$_{one\text{-}case}$* and the *HF-PINN$_{param}$* are presented and discussed in terms of the loss components normalized by the minimum heat potential $U_{\min}$ computed at 25 °C, which is the minimum temperature T_0 of the scan. Then, the results in terms of the estimated heat flux at the final time of simulation are compared with the THEODOR code. Once trained, the models are tested on a uniform grid with 40 points over the tile depth (horizontal axis), 200 points over the tile width (vertical axis), and 30 points over time.

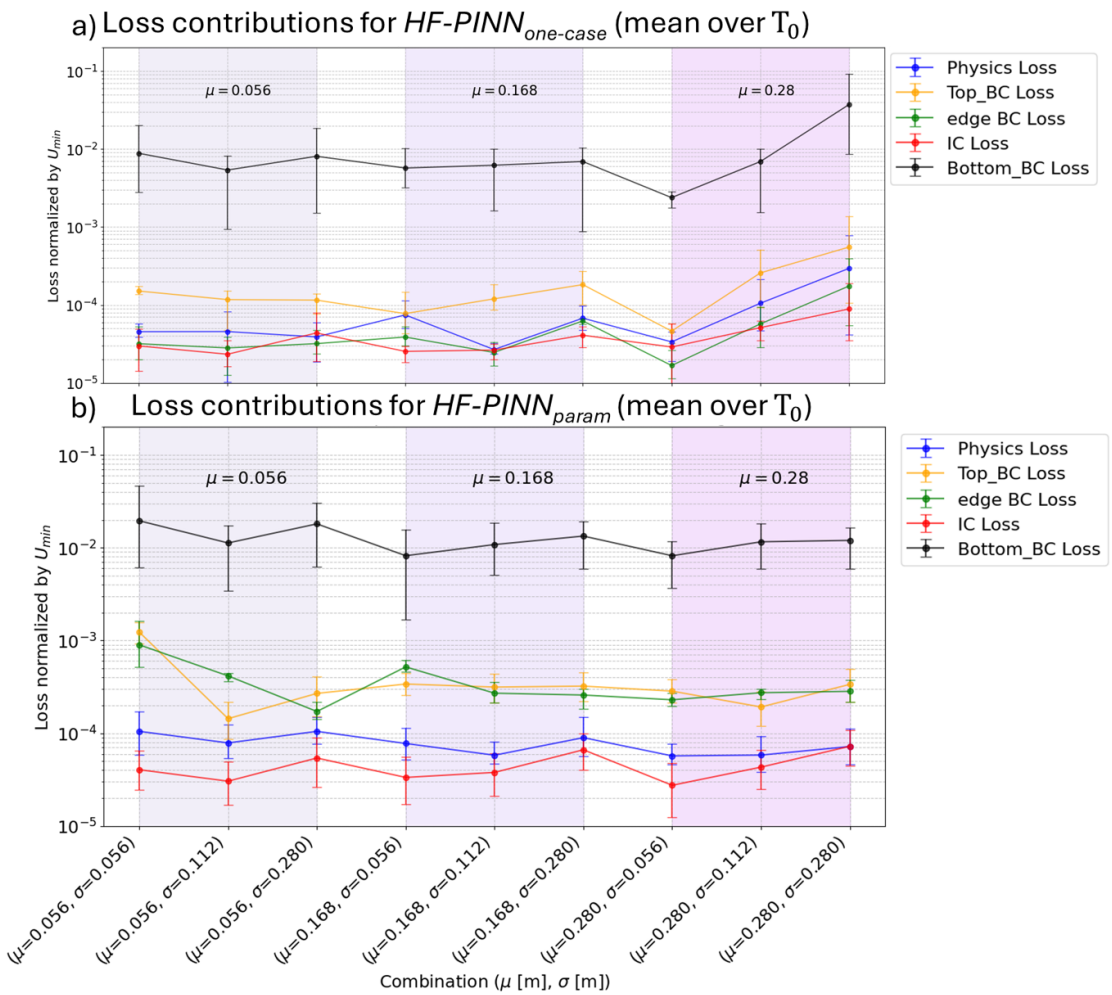

Figure 4. Loss contributions of HF-PINN, where the blue line indicates the physics loss L_{PDE}, the red line the initial condition loss L_{t0}, the green line the edge adiabatic loss L_{bN}, the orange line the top boundary condition loss L_{bD}, and the black line the initial condition loss L_{bR}. The error bar represents the average loss (marker) and the minimum and maximum values (bars) for the losses at $T_0 = [25,\ 100,\ 200]^\circ C$: a) loss contributions for the *HF-PINN$_{one-case}$*; b) loss contributions for the *HF-PINN$_{param}$*.

3.2. HF-PINN$_{one-case}$

Figure 4(a) shows the results of the sensitivity scan in terms of the *HF-PINN* losses. The x-axis reports the different parameter combinations obtained by first varying σ and μ. The T_0 variation is represented by the error bars, where each marker represents the average loss over the three T_0 values and the bars represent the corresponding minimum and maximum values. For this reason, the horizontal axis from left to right reports values with increasing σ. It is possible to notice that the different losses are correlated to each other, and they tend to peak or decrease at the same combinations of (μ, σ), possibly due to the mutual interactions among them. In fact, the top boundary condition can introduce a gradient at the left edge of the tile $(y = 0)$ when μ is low and σ increases (lighter shade of purple in the plot). This causes the adiabatic loss to increase in the left side of the tile, especially close to the top of the tile $(x = 0)$ even if the boundary points at the corner are not sampled to avoid inconsistencies. In conclusion, the top and bottom boundary condition losses, together with the physics loss contribute mostly to the total loss shown in figure 5 (blue line), where all the contributions are summed up plainly, without applying any weight. Note that the bottom boundary condition is less influent than the others to the heat flux estimation task as the surface heat fluxes do not strongly depend on the dissipated heat flow at the bottom for a short simulation time considered in this sensitivity scan.

3.3. HF-PINN$_{\mathbf{param}}$

Figure 4(b) shows the performance of *HF-PINN$_{param}$* over the same set of parameters as *HF-PINN$_{one-case}$*. Figure 4(b) highlights how also in this case, even if the contributions to the loss are still correlated, the bottom boundary condition loss is still the dominant one. Moreover, despite some higher top boundary condition and edge boundary condition losses due to the combination of low σ together with low μ

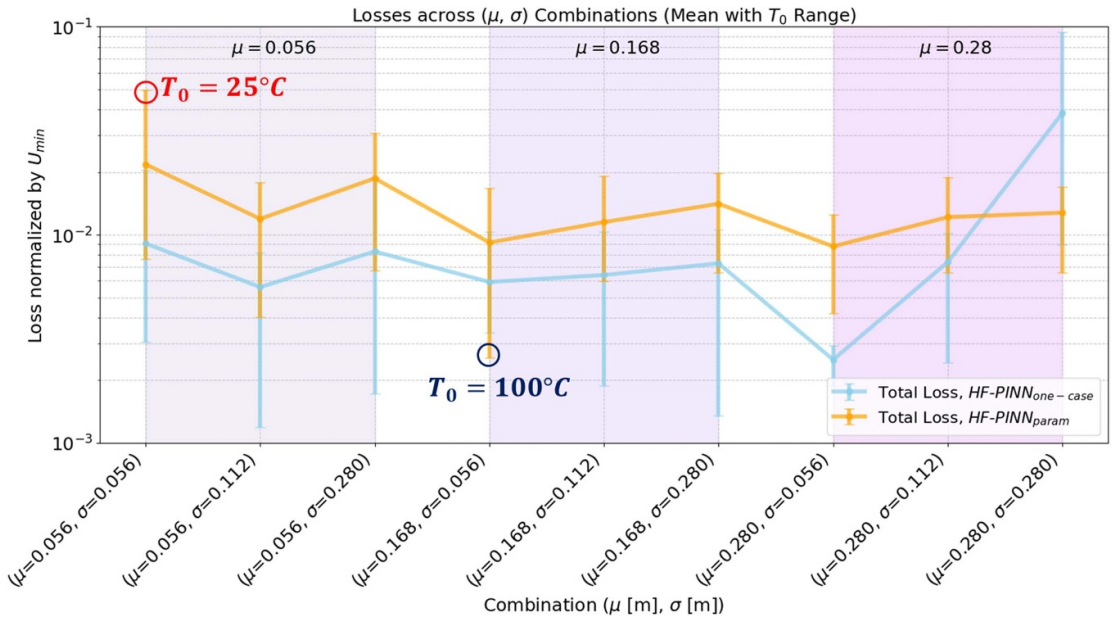

Figure 5. Total loss for the *HF-PINN*$_{one\text{-}case}$ (light blue line), and for the *HF-PINN*$_{param}$ (orange line), obtained by summing all loss components with the same weight. The error bar represents the average loss (marker) and the minimum and maximum values (bars) for the losses at $T_0 = [25,\ 100,\ 200]^\circ C$. The two stars with the dashed lines highlight two combinations of parameters analyzed in figures 6(a) (red circle) and (b) (blue circle).

(visible looking at the points in the first shade of purple), the losses of the *HF-PINN*$_{param}$ are quite stable over all the cases of the sensitivity scan. The first two points of figure 4(b) represent a case where a strong gradient at the top-left edge is applied by the top Dirichlet boundary condition, contradicting the adiabatic lateral Neumann boundary condition. Therefore, the *HF-PINN*$_{param}$ finds a numerical compromise trying to minimize both losses and causing the correlation discussed also for the *HF-PINN*$_{one\text{-}case}$. This aspect is of relevance in view of the application of the *HF-PINN* to experimental conditions, where σ values can reduce below 34 mm [20]. One of the reasons behind this behavior is that lower σ determines higher local gradients in the physics loss and sharper variations in the PDE making learning more difficult in high gradient areas [15, 21]. For the *HF-PINN*$_{param}$, the IC loss is lower for higher initial temperatures. This fact may be related to the rescaling of the loss by $U_{\min}$ during the training phase. In fact, higher initial temperatures determine higher heat potentials and hence higher values of the loss. This effect causes the optimizer to place greater emphasis on cases with higher temperatures. On the other hand, *HF-PINN*$_{one\text{-}case}$ does not show a similar trend due to the rescaling of each model by U_0 during training.

3.4. Comparison of the two approaches

In figure 5 the total loss for the two models is compared when normalized by the minimum heat potential $U_{\min}$ computed at 25 °C. Looking at the blue line in figure 5, it is possible to see that in correspondence of $\mu = 0.056$ the loss is slightly higher than in the cases with larger μ. The comparison highlights how the *HF-PINN*$_{param}$ model is able to maintain a total loss similar to the *HF-PINN*$_{one\text{-}case}$ while learning a parametric problem in terms of the transient heat-diffusion PDE. The *HF-PINN*$_{param}$ maintains a total loss of $\approx 1.5 \cdot 10^{-2}$ on average over all the cases of the sensitivity scan. Figure 6 compares the *HF-PINN*$_{one\text{-}case}$ and *HF-PINN*$_{param}$ for two scenarios taken from figure 5. The first scenario, shown in figure 6(a), concerns heat diffusion with a narrow Gaussian boundary condition applied at the top-left side of the tile ($\mu = 0.056\ m,\ T_0 = 25°,\ \sigma = 0.056\ m$), indicated by the red circle in figure 5. The second case is a heat diffusion with a Gaussian closer to the center of the tile, with the same width of the previous one ($\mu = 0.168\ m, T_0 = 100°C,\ \sigma = 0.056\ m$, indicated with a blue circle in figure 5), which is shown in figure 6(b). The heat flux estimated by *HF-PINN*$_{one\text{-}case}$ is represented by a blue line, the one estimated by *HF-PINN*$_{param}$ is represented by an orange line and THEODOR estimated heat flux is in green, with a shaded area indicating the tolerance of $\pm$ 10%. In both cases, the *HF-PINN*$_{one\text{-}case}$ estimation, is inside the shaded area, but in the figure 6(b), it is possible to appreciate how the interaction between the adiabatic loss at the left side and the shape of the heat flux at the edge of the tile determine a deterioration of the *HF-PINN*$_{one\text{-}case}$ estimation with respect to the THEODOR one. On the

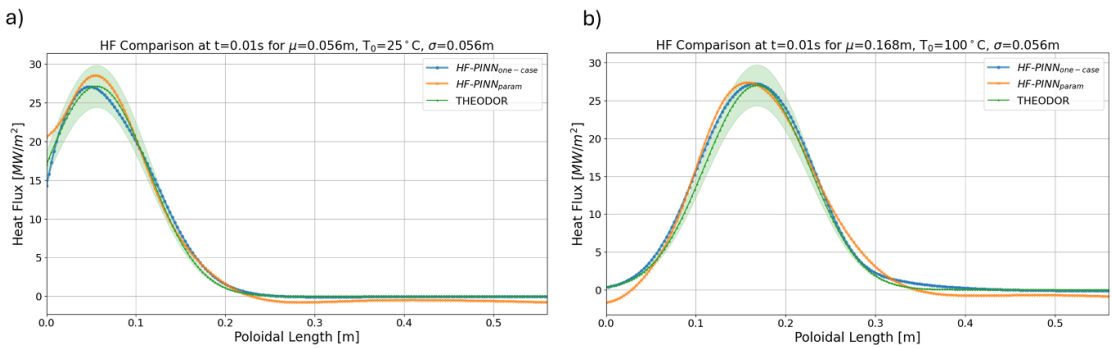

Figure 6. Comparison of the estimated heat flux from *HF-PINN*$_{one\text{-}case}$ (blue line), *HF-PINN*$_{param}$ (orange line) and THEODOR (green line). A shaded green area indicates a 10% margin on the value estimated by THEODOR. The two figures represent case a), where the heat flux is narrow and placed at the lateral edge of the tile ($\mu = 0.056\ m, T_0 = 25°C,\ \sigma = 0.056\ m$) and case b) where the heat flux is placed closer to the center of the tile ($\mu = 0.168\ m, T_0 = 100°C,\ \sigma = 0.112\ m$).

other hand, the *HF-PINN*$_{param}$ is able to reconstruct two very different heat flux behaviors with a parametric approach, despite having a higher error with respect to the *HF-PINN*$_{one\text{-}case}$, specifically trained for finding a specific solution of equation (1) with a fixed boundary condition. A similar deterioration of the performance is shown when comparing a parametric Grad-Shafranov solver against a PINN for the single case in [17]. The normalized mean absolute error (NMAE) is computed comparing the *HF-PINN* estimated heat flux with the THEODOR one with

$$NMAE = \ 100 \cdot \frac{\frac{1}{\mathrm{n}} \sum_{i=1}^{n} \left| q_{true} - q_{pred} \right|}{\frac{1}{n} \sum_{i=1}^{n} \left(q_{true} \right)} \tag{11}$$

where q_{true} are THEODOR estimated values and q_{pred} the values estimated by *HF-PINN*, so that the NMAE provides an estimate of the mismatch between THEODOR estimated and *HF-PINN* predicted heat fluxes. The NMAE varies from a minimum of 2.8% to a maximum of 11.3% for the *HF-PINN*$_{one\text{-}case}$, while these values increase to 9.1% for the minimum and 15.8% for the maximum for the *HF-PINN*$_{param}$. For reference, the NMAE for the example of figure 6(a) of the *HF-PINN*$_{one\text{-}case}$ *is* 5.4% and the one of *HF-PINN*$_{param}$ is 11.4%, while for the example of figure 6(b) the NMAE of the *HF-PINN*$_{one\text{-}case}$ *is* 8% and the one of *HF-PINN*$_{param}$ is 14.2%.

When *HF-PINN* is reconstructing the heat flux in real-time, not only will the heat flux be necessary at the end of the simulation, but the code will also retrieve the temperature in the bulk of the tile, which is used to track the state of the tile in the following code evaluations. For this reason, figure 7 reports the mean absolute error (MAE) computed as

$$MAE = \ \frac{1}{\mathrm{n}} \sum_{i=1}^{n} \left| T_{true} - T_{pred} \right| \tag{12}$$

where T_{true} are THEODOR estimated values and T_{pred} the values estimated by *HF-PINN*. The MAE obtained comparing *HF-PINN*$_{one\text{-}case}$ estimated tile temperature with THEODOR (light blue line) and the MAE on the *HF-PINN*$_{param}$ estimated tile temperature compared with THEODOR (orange line). The values reported are in °C and highlight a low MAE of less than 1.5 °C in all the combinations of the sensitivity analysis, suggesting a low error on the state of the tile at the end of the simulation.

3.5. Computational performance and scalability analysis

The advantage of the HF-PINN is that it can be parallelized with the graphical processing unit, so that it can be faster when processing at the same time large data slices (for instance, multiple tiles at the same time). Since at the moment experimental data are not considered in the analysis, a scan on the number of processed points, increasing the mesh size, has been performed. For each point of the scan, a diffusion step is simulated 40 times with THEODOR and with the HF-PINN, calculating the average elapsed time and its standard deviation, as shown in figure 8. As it is possible to notice, the HF-PINN achieves a speedup of approximately one order of magnitude compared to THEODOR, supporting the potential of the HF-PINN as a viable methodology for real-time applications.

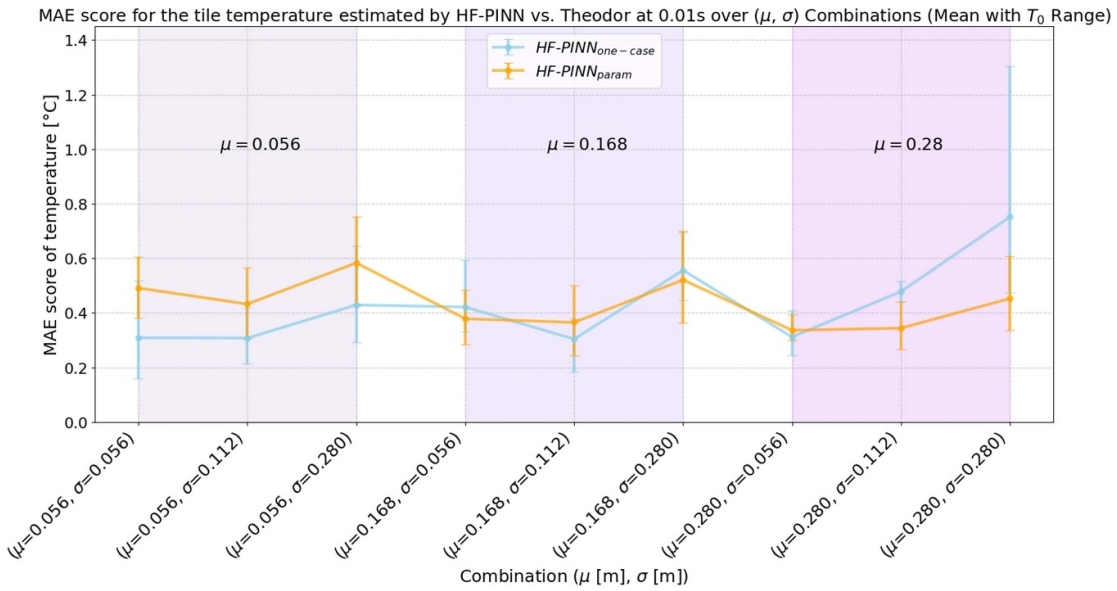

Figure 7. MAE of the *HF-PINN*$_{one\text{-}case}$ estimated tile temperature at the end of the simulation compared with THEODOR (light blue line) and of the *HF-PINN*$_{param}$ estimated tile temperature at the end of the simulation compared with THEODOR (orange line). The error bar represents the average loss (marker) and the minimum and maximum values (bars) for the losses at $T_0 = [25,\ 100,\ 200]^\circ C$.

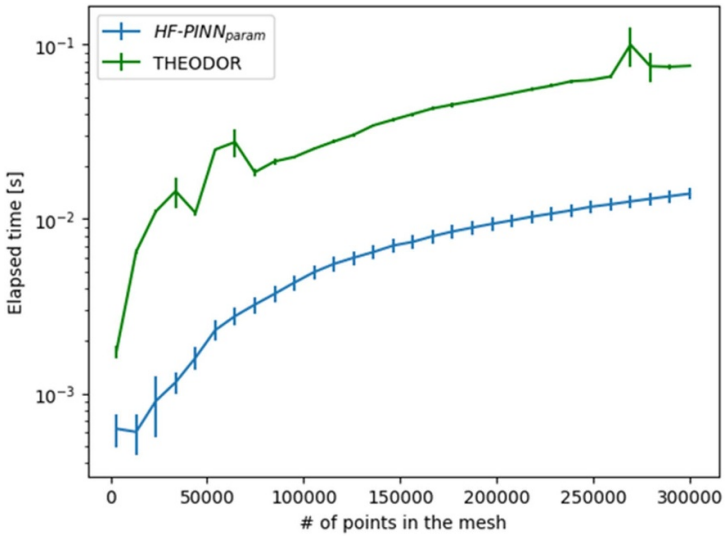

Figure 8. Comparison of the elapsed time for a diffusion step between the HF-PINN$_{\text{param}}$ and THEODOR. The line indicates the average time over 40 computations and the bars the standard deviation.

4. Conclusions and future work

This work investigates the potential of PINNs for their use in the real-time heat flux estimation at W7-X and proposes proof of concept for parametrizing them in view of a real-time application. Firstly, a scan of the possible experimental boundary conditions is made to verify the capability of *HF-PINN*$_{one\text{-}case}$, a PINN trained on the single heat diffusion problem, to learn the evolution of the diffusion problem. Then, a parametric model *HF-PINN*$_{param}$ is developed to learn with a single model the evolution of several transient heat diffusion equations, parametrized depending on the initial temperature T_0 of the tile, the position μ and the standard deviation σ of the Gaussian temperature profile. This model, despite having a larger error than the *HF-PINN*$_{one\text{-}case}$, showed robust performance over all the cases, demonstrating the potential for learning a family of solutions in view of the real-time application with experimental data. Currently, the approach works with a parametrization of the initial temperature value of the tile which is not applicable to the experimental condition in long experiments, but future work will

investigate the extension of the approach for the validated experimental data of the W7-X OP1.2 campaign. The long-term goal is the analysis of the data of the new water-cooled divertor installed for OP2 campaign, which will require the development of a PINN which solves a 3D heat diffusion problem. However, THEODOR is not capable of solving the heat diffusion equation in a multi-layered material as the new W7-X divertor tile. For this purpose, a new code, DELVER, will process the OP2 experimental data modeling the layered structure of the new divertor tiles and solving a 3D diffusion equation [22], hence providing reliable training data for a future 3D PINN.

Acknowledgment

This work has been carried out within the framework of the EUROfusion Consortium, funded by the European Union via the Euratom Research and Training Programme (Grant Agreement No 101052200—EUROfusion). Views and opinions expressed are however those of the author(s) only and do not necessarily reflect those of the European Union or the European Commission. Neither the European Union nor the European Commission can be held responsible for them.

Data availability statement

All data that support the findings of this study are included within the article (and any supplementary files).

Author contributions

Enrico Aymerich 0000-0003-3787-7685
Conceptualization (lead), Data curation (lead), Formal analysis (lead), Funding acquisition (equal), Investigation (lead), Methodology (lead), Project administration (supporting), Resources (equal), Software (lead), Validation (lead), Visualization (lead), Writing – original draft (lead), Writing – review & editing (lead)

Fabio Pisano 0000-0003-0162-0562
Conceptualization (supporting), Formal analysis (supporting), Funding acquisition (supporting), Investigation (supporting), Methodology (supporting), Resources (equal), Supervision (equal), Validation (supporting), Visualization (supporting), Writing – original draft (supporting), Writing – review & editing (supporting)

Giuliana Sias 0000-0002-2289-301X
Conceptualization (supporting), Formal analysis (supporting), Investigation (supporting), Methodology (supporting), Supervision (equal), Validation (supporting), Writing – review & editing (supporting), Funding acquisition (supporting)

Barbara Cannas 0000-0002-2766-0557
Project administration (equal), Supervision (supporting), Validation (supporting), Visualization (supporting), Writing – review & editing (supporting)

Alessandra Fanni 0000-0001-8604-5282
Project administration (equal), Supervision (supporting), Validation (supporting), Visualization (supporting), Writing – review & editing (supporting)

Joris Fellinger 0000-0003-2380-0329
Supervision (supporting), Validation (supporting), Writing – review & editing (supporting)

Yu Gao 0000-0001-8576-0970
Data curation (supporting), Resources (supporting), Supervision (supporting), Validation (supporting), Writing – review & editing (supporting)

Marcin Jakubowski 0000-0002-6557-3497
Resources (supporting), Supervision (supporting), Validation (supporting), Writing – review & editing (supporting)

Sebastian Thiede 0009-0007-8018-8187
Data curation (supporting), Investigation (supporting), Writing – review & editing (supporting)

Table A1. Parameters of the material properties fit.

Parameter	k $[W/(m \cdot K)]$	D $[m^2/s]$
a	19.09	6.64e-06
b	146.5	1.38e-4
τ_0	1088.80	415.89

Appendix A1 Relationship between heat potential and temperature

The W7-X divertor has been modeled as in [11], where, in figure A1 in the Appendix, the properties of the divertor tile are shown. The nonlinear relationship of the thermal conductivity k and the thermal diffusivity D with respect to temperature T is modeled with a hyperbolic inverse-square decay function:

$$f(T) = a + b\left(\frac{\tau_0}{T+\tau_0}\right)^2 \tag{A-1}$$

where T is the temperature in °C, while a, b and T_{c0} are the three parameters of the fit, computed as in [11]. The values of the fit for k and D are reported in table A1.

Renaming these values a_{c0}, b_{c0} and τ_{c0} for the thermal conductivity k and a_{d0}, b_{d0} and τ_{d0} for the thermal diffusivity D, the equation (3) in the work becomes:

$$u(T) = \int_{0°C}^{T} k(T)\,dT = T\left(a_{c0} + \mathrm{b_{c0}}\left(\frac{1}{1+\frac{T}{\tau_{c0}}}\right)\right) \tag{A-2}$$

which leads to the following second order equation

$$a_{c0}T^2 + T((a_{c0}+\mathrm{b_{c0}})\tau_{c0} - \mathrm{u}) - \mathrm{u}\,\tau_{c0} = 0 \tag{A-3}$$

whose positive solution allows to obtain T starting from $u(T)$. Using these concepts, the following losses are converted from temperature into heat potential:

Initial condition (IC): The tile bulk temperature is assumed to be uniform and equal to T_0 at $t = 0$. The corresponding heat-potential initial condition is therefore spatially uniform:

$$\hat{u}(x,y,0) = u_{t0}(x,\ y) = u(T_0) = \int_0^{T_0} k(T')\,dT' \tag{A-4}$$

Dirichlet boundary condition (BC) on the tile top surface ($x = 0$): The IR-camera measurement of the surface temperature $T_{\mathrm{bD}}(y,t)$ enforces the top BC. In the heat-potential formulation this reads:

$$\hat{u}(0,y,t) = u_{bD}(y,\ t) = u(T_{bD}(y,\ t)) = \int_0^{T_{bD}(y,\ t)} k(T')\,dT' \tag{A-5}$$

Neumann BC on the tile lateral edges ($y = 0$ and $y = y_{\max}$): Adiabatic conditions are imposed, expressed directly in heat-potential form as:

$$\frac{\partial \hat{u}}{\partial y}(x,\ 0,\ t) = \frac{\partial \hat{u}}{\partial y}(x,\ y_{max},\ t) = 0 \tag{A-6}$$

Bottom boundary condition ($x = x_{\max}$): For the inertially cooled divertor considered in this work, the Robin boundary condition is imposed similarly to the Neumann one, by comparing the normal heat flux with the convection term. However, the bottom temperature is computed inverting the integral in equation (3):

$$\frac{\partial \hat{u}}{\partial x}(x_{max},y,t) = \alpha_{bottom}\left(\hat{T}(x_{max},y,t) - T_{cool}\right) \tag{A-7}$$

where $\hat{T}(x_{\max},y,t)$ is obtained from the positive solution of:

$$a_{c0}\hat{T}^2 + \hat{T}((a_{c0}+\mathrm{b_{c0}})\tau_{c0} - \hat{u}) - \hat{u}\,\tau_{c0} = 0 \tag{A-8}$$

where $\hat{u}$ is the HF-PINN estimated heat potential.

References

[1] Sunn Pedersen T *et al* 2019 First divertor physics studies in Wendelstein 7-X *Nucl. Fusion* **59** 096014
[2] Niemann H *et al* 2020 Large wetted areas of divertor power loads at Wendelstein 7-X *Nucl. Fusion* **60** 084003
[3] Effenberg F *et al* 2019 Investigation of 3D effects on heat fluxes in performance-optimized island divertor configurations at Wendelstein 7-X *Nucl. Mater. Energy* **18** 262–7
[4] Zhou S *et al* 2022 Equilibrium effects on the structure of island divertor and its impact on the divertor heat flux distribution in Wendelstein 7-X *Nucl. Fusion* **62** 106002
[5] Grulke O *et al* 2024 Overview of the first Wendelstein 7-X long pulse campaign with fully water-cooled plasma facing components *Nucl. Fusion* **64** 112002
[6] Xu S *et al* 2023 Modeling of plasma beta effects on the island divertor transport in the standard configuration of W7-X *Nucl. Fusion* **63** 066005
[7] Schmitz O *et al* 2020 Stable heat and particle flux detachment with efficient particle exhaust in the island divertor of Wendelstein 7-X *Nucl. Fusion* **61** 016026
[8] Jakubowski M *et al* 2021 Overview of the results from divertor experiments with attached and detached plasmas at Wendelstein 7-X and their implications for steady-state operation *Nucl. Fusion* **61** 106003
[9] Aymerich E *et al* 2023 Physics informed neural networks towards the real-time calculation of heat fluxes at W7-X *Nucl. Mater. Energy* **34** 101401
[10] Pisano F, McFadden G B and Cerfon A J 2020 Learning control coil currents from heat-flux images using convolutional neural networks at Wendelstein 7-X *Plasma Phys. Control. Fusion* **62** 044002
[11] Gao Y, Jakubowski M W, Drewelow P, Pisano F, Puig Sitjes A, Niemann H, Ali A and Cannas B 2019 Methods for quantitative study of divertor heat loads on W7-X *Nucl. Fusion* **59** 066007
[12] Herrmann A, Junker W, Gunther K, Bosch S, Kaufmann M, Neuhauser J, Pautasso G, Richter T and Schneider R 1995 Energy flux to the ASDEX-Upgrade diverter plates determined by thermography and calorimetry *Plasma Phys. Control. Fusion* **37** 17–29
[13] Sieglin B *et al* 2015 Real time capable infrared thermography for ASDEX Upgrade *Rev. Sci. Instrum.* **87** 113502
[14] Herrmann A 2001 Limitations for divertor heat flux calculations of fast events in tokamaks (available at: https://api.semanticscholar.org/CorpusID:118686733)
[15] Rathore P, Lei W, Frangella Z, Lu L and Udell M 2024 Challenges in training PINNs: a loss landscape perspective (arXiv:2402.01868)
[16] Li S and Feng X 2022 Dynamic weight strategy of physics-informed neural networks for the 2D Navier–Stokes equations *Entropy* **24** 1254
[17] Jang B, Kaptanoglu A A, Gaur R, Pan S, Landreman M and Dorland W 2024 Grad–Shafranov equilibria via data-free physics informed neural networks *Phys. Plasmas* **31** 032510
[18] McFall K S and Mahan J R 2009 Artificial neural network method for solution of boundary value problems with exact satisfaction of arbitrary boundary conditions *IEEE Trans. Neural Netw.* **20** 1221–33
[19] Lagaris I E, Likas A and Papageorgiou D G 2000 Neural-network methods for boundary value problems with irregular boundaries *IEEE Trans. Neural Netw.* **11** 1041–9
[20] Dräger S, Kremeyer T, Gao Y, Wolf R and Reimold F 2024 Quantification and analysis on the formation of a secondary strike line in the Wendelstein 7-X stellarator presented at the DPG-Frühjahrstagung der Sektion Materie und Kosmos (SMuK) DPG (available at: https://hdl.handle.net/21.11116/[0000-0010]-F9A6-A) (Accessed 23 Jan 2026)
[21] Gopakumar V, Pamela S and Samaddar D 2023 Loss landscape engineering via data regulation on PINNs *Mach. Learn. Appl.* **12** 100464
[22] Thiede S, Gao Y, Stiegliz D, Jakubowski M, Krause M and Manz P 2026 Improving heat flux calculations for the non-axisymmetric loads on plasma facing components in Wendelstein 7-X *Rev. Sci. Instrum.* **97** 043504